Nanoscale

PAPER

View Article Online
View Journal | View Issue

Cite this: *Nanoscale*, 2022, **14**, 17372

A multi-chromic supercapacitor of high coloration efficiency integrating a MOF-derived V_2O_5 electrode†

Anweshi Dewan,[a] Remya Narayanan[b] and Musthafa Ottakam Thotiyl *[c]

Received 3rd September 2022,
Accepted 10th November 2022

DOI: 10.1039/d2nr04841h

rsc.li/nanoscale

Modern technological trends in smart electronic devices demand more intelligent automation. Simultaneous integration of energy storage and multicolor electrochromism in a single device improves user–device interfacing based on a salient human-readable output. In this work, primarily metal–organic framework (MOF) derived V_2O_5 was synthesized which, as an electrochromic material, shows high optical modulation of 35% at 485 nm, with very fast switching speeds (2.9/3.4 s for coloring/bleaching). The multiple coloration states of the V_2O_5 electrode make it worthy for further integration as a smart negative electrode in a multicolored electrochromic asymmetric supercapacitor, where the electrochromic polyaniline electrode serves as the counter electrode. The device demonstrates a high coloration efficiency of 137.2 $cm^2\ C^{-1}$ and an areal capacitance of 12.27 mF cm^{-2} and an energy density of 2.21 × 10^{-3} mW h cm^{-2} at a current density of 0.05 mA cm^{-2}. By virtue of its different chromatic states during charging and discharging, smart visual tracking of the state of charge of the supercapacitor can be realized. Such a design of energy storage devices will have promising practical application in futuristic smart multifunctional electronic devices.

1. Introduction

Major environmental concerns due to global climate change impel us towards the use of alternative energy sources with a low carbon footprint.[1,2] Consequently, the 21st century science community is crucially focused towards zero emission technologies like solar cells, batteries, supercapacitors (SCs), fuel cells, *etc*. to ameliorate the quality of life.[3–6] Electrochemical capacitors or supercapacitors (SCs) have gained widespread attention due to their fast charge–discharge rate and long life along with important advantages to meet the urgent demand of high power density.[7,8] With the recent evolution of electronic devices, the applications of SCs have been extended to multi-functional and smart devices like self-charging SCs,[9] flexible and wearable SCs,[10] shape-memory SCs,[11] thermo-responsive SCs,[12] self-healable SCs,[13] electrochromic SCs (ECSCs),[14,15] *etc*. Materials whose redox reaction leads to a visual color change are known as electrochromic materials and offer opportunities for bridging electrochromism with the state of charge of supercapacitors.[16,17] These devices are concurrently capable of efficient energy management as the expended energy during the charging process can be retrieved at the time of bleaching. By exploiting the configuration of an asymmetric SC, these devices could be implemented in different applications including smart windows for indoor light and temperature controls, adaptive camouflages, aesthetic multicolor displays with energy storage functionality, *etc*. Multi-colored electrochromic asymmetric supercapacitors (MECASCs) with different chromatic states will allow precise control over the modulation of light along with the real-time monitoring of the charge content of the device for its sustainable use by averting overcharging and over-discharging.[18–20]

There exist different electrochromic (EC) materials including organic molecules like viologens,[21] conducting polymers (CPs),[22] Prussian blue,[23] transition metal oxides (TMOs),[24–26] *etc*. The most studied EC materials are based on TMOs and CPs. Reportedly, a CP such as polyaniline (PANI) is of great interest due to its low cost, ease of synthesis, high electrical conductivity, rich color states, high theoretical capacity, *etc*.[27] On the other hand, TMOs have emerged as the protagonist in the field of electrochromism owing to their superb optical memory effect, environmental stability and natural abundance.[28] Among the TMOs, V_2O_5 is highly sought after in the

[a]*Department of Physics and Centre for Energy Science, Indian Institute of Science Education and Research Pune, 411008, India*
[b]*Department of Environmental Science, Savitribai Phule Pune University, Pune, 411007, India*
[c]*Department of Chemistry and Centre for Energy Science, Indian Institute of Science Education and Research Pune, 411008, India. E-mail: musthafa@iiserpune.ac.in*
†Electronic supplementary information (ESI) available. See DOI: https://doi.org/10.1039/d2nr04841h

field of electrochromism as it is the only TMO that can demonstrate both anodic and cathodic coloration upon reversible intercalation/deintercalation of alkaline cations (*e.g.*, Li^+), which makes it suitable for multicolor displays. In addition, it has high theoretical capacity which makes it a strong contender for a wide variety of electrochemical applications.[29]

However, bulk V_2O_5 often suffers from serious volume expansion over cycling, poor ion diffusion kinetics, long switching times, low electrical conductivity, *etc*.[30] To overcome these limitations, a lot of research has been carried out to make different micro-nanostructures of V_2O_5 and hybrid materials by the incorporation of carbonaceous materials into them.[31,32] Recently, metal–organic frameworks (MOFs) have been used as a template for the synthesis of TMOs. MOFs are an emerging class of hybrid crystalline materials assembled *via* the coordination bonds between organic ligand molecules and metal ion centers, with huge chemical and configurational heterogeneities. These materials possess very high surface areas and tunable pore sizes. Owing to their long range ordered porous structure with periodically arranged metal clusters, MOFs are used as sacrificial templates in the synthesis of porous metal oxides, sulfides and porous carbon embedded hybrid materials including V_2O_5.[33–39]

In the present work, we show a MECASC constructed by stacking MOF-derived V_2O_5 and PANI films as the negative and positive electrodes respectively in propylene carbonate (PC) solvents containing 1 M $LiClO_4$ as the electrolyte. The module visually exhibits the stored energy level by different colors as well as demonstrates the feasibility of redemption of the acquired energy during bleaching. MOF-derived V_2O_5 samples are synthesized by two different pyrolysis procedures. Carbon leftovers along with the porous structures of the V_2O_5 samples provide the ions of the electrolyte hassle-free access to the reaction sites to enhance the charge transfer kinetics. Thorough electrochemical characterization of the V_2O_5 electrodes and separately the capacitance measurements of both V_2O_5 and PANI electrodes are carried out in 1 M $LiClO_4$/PC medium in a three-electrode setup. In a two-electrode configuration, a functional MECASC device is fabricated having a wide potential window up to 2 V with the option to visually judge the state of charge of the device.

2. Experimental section

2.1. Chemicals

Vanadium trichloride (VCl_3), *p*-benzenedicarboxylic acid (PTA), aniline, *N*,*N*-dimethylformamide (DMF), propylene carbonate (PC) and lithium perchlorate ($LiClO_4$) were acquired from Alfa Aesar. Transparent SnO_2 : F (FTO) coated glass substrates with a sheet resistance of 15 Ω sq^{-1} were obtained from Sigma Aldrich. All the chemicals were of analytical grade and used as received without any further modification. FTO substrates were washed with soap solution, and later rinsed with isopropanol, ethanol and an ample amount of water, respectively, under ultrasonic treatment. During the experiments, aqueous solutions were prepared using reagent grade Milli-Q water with 18.2 MΩ cm resistivity (Millipore Direct Q3 system).

2.2. Material synthesis and electrode fabrication

2.2.1. Synthesis of a negative electrode material (V_2O_5). MIL-101(V) (vanadium MOF or V-MOF) was synthesized *via* a solvothermal reaction route following the report of Carson *et al.*[40] According to the report, 166 mg of PTA (1 mmol) and 157 mg of VCl_3 (1 mmol) were first added to 5 ml of absolute ethanol. The mixture was then kept on a Tarson 3002 Spinix vortex shaker for 10 min, until the solution turns green. Then the whole precursor solution was transferred to a 30 ml Teflon-lined autoclave. The autoclave was then heated in an oven at 120 °C for 48 h. After the reaction was complete, the autoclave was very slowly cooled down to room temperature (slow cooling is very important to obtain a crystalline MOF). The obtained product was then washed with ethanol and separated by centrifugation. The activation of the MOF was performed by heating it in DMF under N_2 gas flow for 3 h at 70 °C, followed by subsequent heating in ethanol for 3 h at 70 °C under N_2 flow. Finally, the obtained green product was dried under vacuum at 120 °C for 16 h, which resulted in the formation of a fluffy green V-MOF powder. To further obtain V_2O_5 from the V-MOF, two different annealing procedures were followed. In the first procedure, according to the report of Liang *et al.*,[28] a two-step pyrolysis technique was followed where in the 1st step V-MOF powder was transferred to a ceramic boat before being transferred to a tube furnace, where it was annealed at 370 °C for 1 h under Ar–H_2 (97-3) flow and in the 2nd step the sample was subjected to another heat treatment for 30 min under air flow to obtain the product, designated as V_2O_5-2 throughout this article. Furthermore, in the second procedure, the V-MOF was directly annealed at 370 °C for 30 min under air. The product obtained by this process is labelled here as V_2O_5-1.

2.2.2. Fabrication of V_2O_5 films on FTO. All V_2O_5 films in this work were prepared on FTO using spray coating. The dispersion required for spray coating was prepared by dispersing the samples in an isopropanol and Milli-Q water mixture. Part of the substrates was covered with Scotch tape to fix the geometrical area of the electroactive material on the electrode. Subsequently, the dispersion was spray-coated on FTO kept on a hot plate at 70 °C with an air-brush (ANMSALES AB-130, nozzle diameter ~0.3 mm; purchased from Amazon) using Ar as a carrier gas at a fixed pressure. The gap between the FTO and airbrush nozzle was maintained to be ~12 cm. After each spray, adequate time was provided to dry the FTO.

2.2.3. Synthesis of a positive electrode material (PANI). PANI was deposited on FTO substrates by the electrodeposition technique following the report of Mohd *et al.*[41] An electrolyte solution of 0.5 M aniline in 1 M H_2SO_4 was used for the deposition. Upon application of a positive bias, aniline monomers get oxidized to radical ions triggering the polymerization reaction to occur.[42] All films were deposited for 150 s at +0.75 V using a potentiostatic technique in a three-electrode system with Pt wire as the counter electrode and Ag/AgCl/Cl^- as the reference electrode. After deposition, the films were washed

with a copious amount of Milli-Q water and dried under vacuum at room temperature.

2.3. Material characterization and electrochemical measurements

The morphological characterization of the samples was performed by field emission scanning electron microscopy (FESEM, Zeiss Ultra Plus) and transmission electron microscopy (TEM, JEOL JEM-2200FS operating at 220 kV). Powder XRD measurements were carried out using a Bruker D8 Advanced X-ray diffractometer with Cu Kα radiation (1.54 Å). Thermogravimetric analysis (TGA) was performed using a NETSZCH TGA-DSC system and the samples were heated under ambient atmosphere from room temperature to 600 °C at a rate of 5 °C min^{-1}. The Raman spectroscopy experiment was conducted in a LabRAM HR 800 (HORIBA Jobin Yvon) setup, using a He–Ne Laser (632 nm, working at 10% power). X-ray photoelectron spectroscopy (XPS) measurements of V_2O_5 samples were carried out using monochromatic and micro-focused Al Kα radiation with an energy of 1486.6 eV (Thermo Kalpha+ spectrometer). The BET surface area was measured using a Micromeritics ASAP 2460 volumetric gas adsorption analyzer instrument with liquid N_2 at a temperature of 77 K. Before measurement, all samples were heated at 120 °C for 12 h under vacuum for removing impurities and pore opening.

The electrochemical measurements were carried out in the CH instrument setup (CHI760E). For *in situ* spectro-electrochemistry data, an Ocean Optics setup consisting of a deuterium–halogen light source (DH-2000-BAL), optical fibers (200 μm core diameter) and a spectrometer (FLAME-T-XR1-ES) was used. In all electrochromic and energy storage related measurements, 1 M $LiClO_4$ in PC was used as the electrolyte. For all three-electrode based experiments, FTO plates spray-coated with V_2O_5 or electro-deposited PANI films on FTOs were utilized as working electrodes, and platinum (Pt) wire and silver (Ag) wire were employed as the counter and reference electrodes, respectively.

3. Results and discussion

3.1. Negative electrode material (V_2O_5)

3.1.1. Structural and morphological properties. The XRD pattern of the activated V-MOF is presented in Fig. 1a, which matches well with the reported simulated XRD pattern (CCDC No. 605510).[40,43,44] Before going ahead with the samples for further processing, TGA/DSC measurements were performed. As can be seen from Fig. S1,† the initial weight loss of the sample between 30 and 100 °C was ascribed to the desorption of adsorbed water and solvent molecules. The weight loss of 14.4% in between 100 and 300 °C was attributed to the decoordination of H_2O molecules from the vanadium trimers and the removal of guest molecules from the pores of the MOF structures. Finally, a weight loss of 52% beyond 300 °C leads to the decomposition of the structures and removal of the carbon skeleton towards the formation of fluffy yellow V_2O_5 samples.[37,40] In differential scanning calorimetry (DSC) measurement, the said change in the material is also reflected as a strong endothermic peak centered at ~370 °C indicating the structural collapse of the MOF during the formation of V_2O_5. Fig. 1b presents the XRD data of V_2O_5 samples. XRD patterns of both 1 step and 2 step annealed samples match well with the orthorhombic V_2O_5 phase (JCPDS Card No. 01-072-0433), indicating the crystalline nature of the samples.

Morphological characterization of the samples was conducted by FESEM and TEM measurements. Fig. 1c illustrates the morphology of the V_2O_5-1 sample and the sample mainly consists of irregularly shaped V_2O_5 nanoplates of dimensions ranging between 30 and 90 nm. A lower magnification TEM image is presented in Fig. 1d, which is concurrent with the FESEM images, exhibiting the presence of very thin nanoplates in the sample. The high-resolution TEM (HR-TEM) data (Fig. 1e) of the sample depicts the presence of lattice fringes with spacings of 0.35 and 0.6 nm which correspond to the (210) and (200) crystal planes of orthorhombic V_2O_5, respectively. A similar sort of morphology was also observed for the V_2O_5-2 sample, as illustrated in Fig. S2a–2c.† Furthermore, EDX mapping measurements were performed on both samples to check the presence of different elements *e.g.*, elemental carbon along with vanadium and oxygen as shown in Fig. 1f–i (and in Fig. S2d–2g†). Carbon mapping images (Fig. 1i and Fig. S2g†) of both samples look almost similar and a very small amount of carbon was observed. The amount of carbon in both samples was quantified using XPS measurements as discussed later.

Raman spectroscopy measurements were carried out on both samples. Raman spectra (Fig. S3†) highlight several well-resolved peaks at ~145, 199, 286, 305, 405, 482, 527, 703 and 995 cm^{-1} which are the characteristic peaks of crystalline V_2O_5. The vibrational Raman active modes are associated with vanadium–oxygen–vanadium bending vibrations, translational modes and vanadium–oxygen stretching modes. The highest intensity peak centered at 145 cm^{-1} corresponds to the bond deformation between different molecular units in the plane of layers, also termed the skeleton bending vibration. The peak at 995 cm^{-1} is attributed to the stretching mode vibration related to the V═O bond.[45]

The surface chemical states of the V_2O_5 samples were analyzed through XPS measurements as presented in Fig. 1j–m and Fig. S4.† Fig. 1j and Fig. S4a† present the survey spectra of the samples which show the peaks corresponding to the vanadium, oxygen and carbon in the sample in accordance with the EDX mapping data (Fig. 1f–i). From XPS measurement, the carbon content in V_2O_5-1 and V_2O_5-2 samples were quantified and found to be almost in the similar range of 12.43% and 12.47%, respectively. The core level spectra of V 2p show two major peaks at 517.2 eV and 524.8 eV, which correspond to V $2p_{1/2}$ and V $2p_{3/2}$ (Fig. 1k and Fig. S4b†). On deconvolution, the weaker and broader peaks at 516.3 eV and 523.6 eV are related to the presence of V^{4+} oxidation states and the relatively stronger peaks (at 517.3 and 524.9 eV) are assigned to

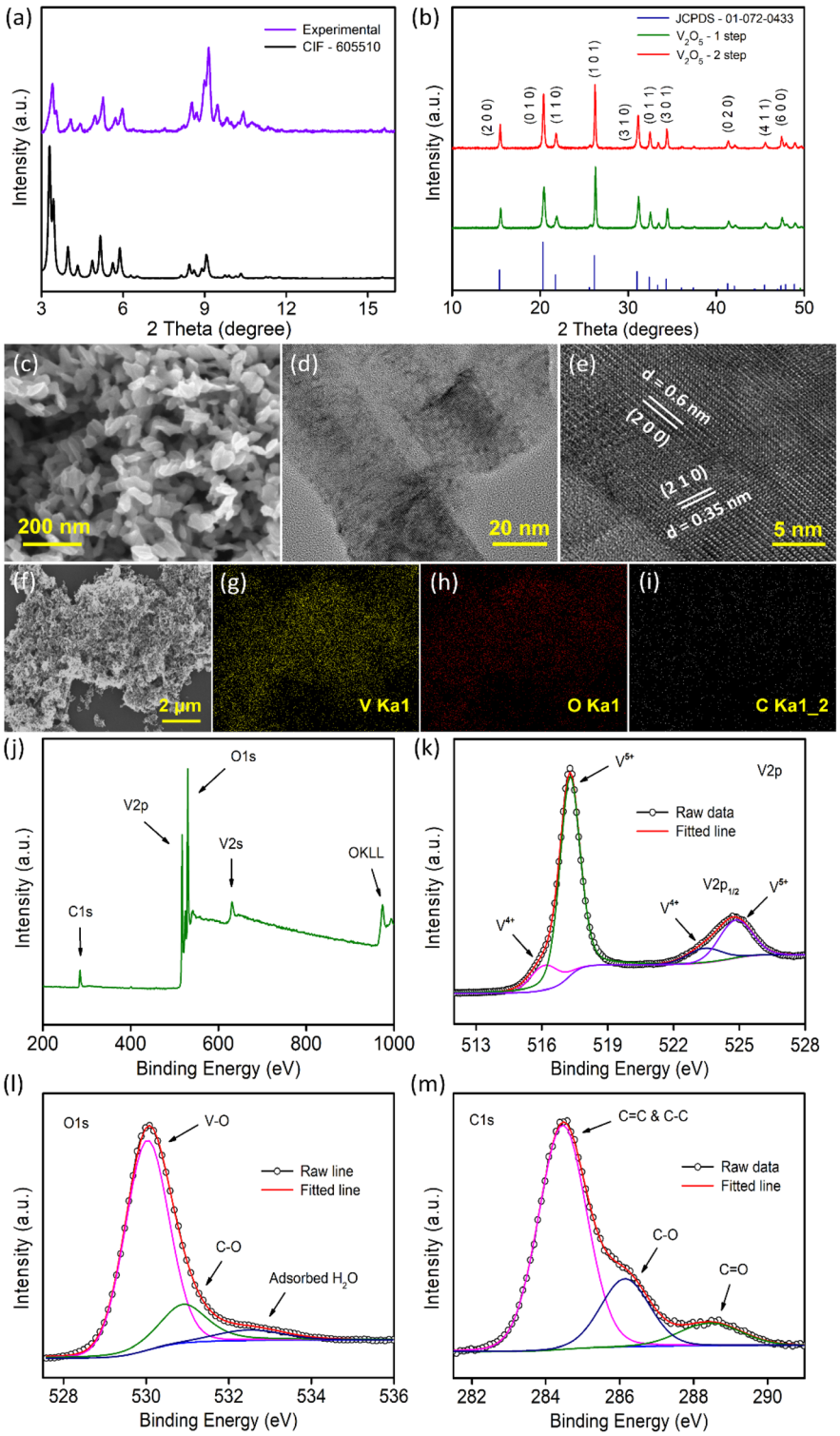

Fig. 1 (a) XRD pattern of the activated V-MOF (purple) and the reported data CIF – 605510; (b) XRD data of V_2O_5 samples along with JCPDS card (01-072-0433) data; (c) FESEM image, (d) TEM image, (e) HRTEM image of the V_2O_5-1 sample and (f–i) EDX data for its elemental mapping, (j) XPS survey spectrum of the V_2O_5-1 sample and deconvoluted XPS spectra of (k) V 2p, (l) O 1s and (m) C 1s levels.

the V^{5+} states of V_2O_5.[35,36,46] The O 1s spectra provided in Fig. 1l and Fig. S4c† can be deconvoluted into three peaks. The most intense peak at 530 eV corresponds to the existence of the V–O bond in V_2O_5. The peak that appeared at 531 eV is due to the C–O bond and the peak that emerged at 532.6 eV is related to either O=C–O or the adsorbed H_2O molecules.[35,47–49] Fig. 1m and Fig. S4d† present asymmetric C 1s peaks, which were resolved into three peaks. The dominant

peak at 284.5 eV arises due to the presence of graphitized carbon (C–C and C=C) in the sample generated due to the denaturation of the carbon skeleton during the annealing of the sample. The peak located at 286.1 eV is associated with the C–O bonds and the smallest peak at 288.5 eV is related to the C=O groups.[48,50] Therefore, XPS data conclude the presence of graphitized carbon in both samples in similar quantities.

Furthermore, N_2 gas adsorption measurement (Fig. S5†) at 77 K was carried out to check the surface areas and pore size distributions of the V_2O_5 samples. The adsorption isotherms exhibit the typical mesoporous nature of the samples. The surface areas of the samples were calculated using the Brunauer–Emmett–Teller (BET) fitting (Fig. S5b and S5e†) and the specific surface area was found to be higher (178 $m^2\ g^{-1}$) for the V_2O_5-1 sample than for the V_2O_5-2 sample (112 $m^2\ g^{-1}$). The non-local pore size distribution (NLDFT) method was used to calculate the pore-size distribution of the samples as shown in Fig. S5c and S5f.† A longer annealing time of V_2O_5-2 (because of the 2-step annealing process) reduces the pore volume in comparison to the only air annealed V_2O_5-1 sample. Overall, the mesoporous structures of the samples are expected to ensure facile ion exchange with the electrolyte towards better electrochemical performance.

3.1.2. Electrochromic studies on V_2O_5 electrodes. The electrochromic properties of V_2O_5 electrodes were examined in a three-electrode setup as mentioned in the Experimental section using an *in situ* spectroelectrochemical technique. Before analyzing the spectro-electrochemistry data, we investigated the electrochemical process, responsible for the electrochromism of V_2O_5. The whole process of reversible colour change is mostly dependent on the reversible Li^+ ion intercalation and deintercalation in V_2O_5 electrodes causing a redox reaction which leads to a change in the oxidation state of vanadium and consequently to different chromatic states. In Fig. 2a, the cyclic voltammograms (solid line) (CV) of the V_2O_5-1 electrode at a scan rate of 7 mV s^{-1} features two pairs of redox peaks and the corresponding electrochemical reaction is stated as follows:[51]

$$V_2O_5 + xLi^+ + xe^- \leftrightarrow Li_xV_2O_5\ (0 \le x \le 1) \qquad (1)$$

where x is the mole fraction of the intercalated Li^+ ions. Based on the amount of inserted Li^+ ions, different crystal phases of V_2O_5 are designated. The 1st redox couple corresponds to the change of α-V_2O_5 ($0 < x < 0.1$) to ε-V_2O_5 ($0.35 < x < 0.5$) and the 2nd redox couple is ascribed to the conversion of ε-V_2O_5 to δ-V_2O_5 ($0.9 < x < 1$) and *vice versa*.[52,53]

The transmission spectra of V_2O_5 samples were collected at different voltages during the cathodic scan (+1 V to −1 V *vs.* Ag/Ag^+ electrode). Fig. 2b illustrates the transmission spectra of V_2O_5-1 electrodes. The corresponding photographs of the films at different voltages are shown in Fig. S6a.† The film reversibly switches its color from yellow (+1 V) to bluish gray (−1 V). Fig. 2c shows the transmission spectra at those two extreme potentials along with the optical modulation data (blue curve), which is defined as the difference between the transmittance at the colored and bleached states of an electrochromic material at a particular wavelength λ (*i.e.*, $\Delta T = T_b(\lambda) - T_c(\lambda)$). The analogous data for V_2O_5-2 electrodes are given in Fig. S6b.† Interestingly, it was observed for both the materials that the transmittance in the visible and near infrared regions changes reversibly upon applying voltages. Higher ΔT values

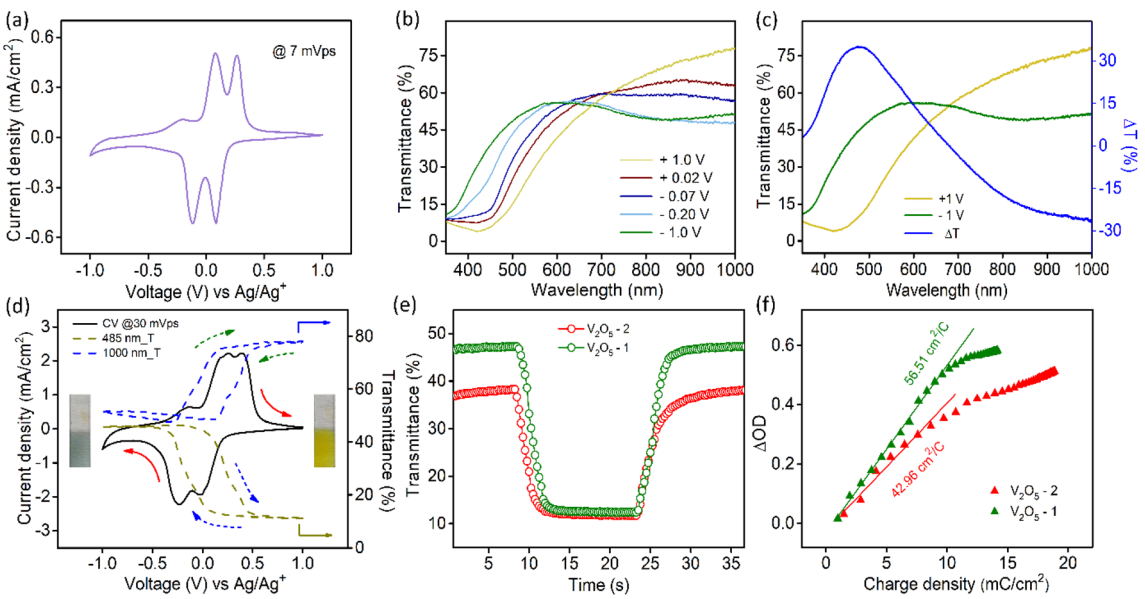

Fig. 2 (a) Cyclic voltammogram (CV) of the V_2O_5-1 electrode in a three-electrode setup at a scan rate of 7 mV s^{-1} in a 1 M $LiClO_4$/PC electrolyte, (b) transmission spectra of V_2O_5-1 films under different biases, (c) transmission of V_2O_5-1 films at two extreme potentials along with the transmission modulation spectrum (ΔT) (blue line), (d) CV data (solid line) of the V_2O_5-1 film with *in situ* transmittance data (dashed lines) at 485 nm (dark yellow) and at 1000 nm (blue), (e) switching times of V_2O_5-1 and V_2O_5-2 at 485 nm under an alternating potential with 15 s interval, and (f) coloration efficiency plot of both the samples.

of about 35% at 485 nm and 26.5% at 1000 nm were obtained for V_2O_5-1 electrodes. In the *in situ* spectroelectrochemistry measurement, the transmission modulation of the V_2O_5-1 film was closely monitored at 485 nm and 1000 nm, as illustrated in Fig. 2d (dotted lines). The dynamical changes of transmittances (indicated by arrows) are commensurate with the modulation of the current density.

Switching time for the electrochromic materials is described as the time required for attaining 90% of the total optical modulation under the application of an alternating potential. Switching times were measured at 485 nm (Fig. 2e) and 1000 nm (Fig. S7a†) wavelengths separately by applying +1 V and −1 V bias. The data for both samples are presented in Table 1. Although each sample contains graphitized carbon almost in close quantity; because of the higher surface area of the V_2O_5-1 sample, it manifests faster switching times compared to the V_2O_5-2 electrodes. The coloration efficiency (CE) of an electrochromic material is an important parameter in terms of estimating the power requirement for electrochromic switching. This is defined as the ratio of the change in the optical density (ΔOD) to the intercalated or deintercalated charge density (mC cm^{-2}).[54] CE can be calculated from the following formula stated as:

$$\mathrm{CE} = \log\,(T_b/T_c)/(Q/A) \quad (2)$$

CE values were calculated at 485 nm and 1000 nm from the slope of the ΔOD *vs.* charge density graphs, as shown in Fig. 2f and Fig. S7b.† The obtained CE values for both material electrodes are presented in Table 1. V_2O_5-1 electrodes excel over V_2O_5-2 electrodes, since their higher surface area provides a lot more active faradaic sites for facile electrochemical reactions.

3.1.3. Electrochemical impedance spectroscopy (EIS) measurement on V_2O_5 electrodes. EIS measurements were conducted in a three-electrode setup for a better understanding of the charge transfer kinetics of V_2O_5 electrodes. The study was performed using an AC signal of 10 mV amplitude with a frequency range of 10 mHz to 100 kHz at the open circuit voltage. Fig. S8a† presents the Nyquist plots along with the fitted data. An equivalent circuit was used for modelling the EIS data (Fig. S8b†), where W is the Warburg impedance, Rs denote resistances and Qs denote the constant phase elements (CPEs) which actually refer to the non-ideality of the electrodes. It is defined as $Q = (Q_0 \times (j\omega)^{\alpha})^{-1}$, where, Q_0 is the pseudo-capacitance and α is a dimensionless parameter, which accounts for the non-ideality, when α is 0, it is purely resistive and for ideal capacitors α is 1.[55] R_1 in the circuit is attributed to the bulk solution resistance. The depressed semicircles in high and medium frequency regions of the spectra are due to two different types of charge propagation phenomena within the system. The first process, modelled with a resistor (R_2) in parallel to a CPE (Q_1) in the high frequency region is either related to the passage of Li^+ ions through a passivation film or through the electrode/electrolyte interface. The resistance R_2 arises due to the mismatch in conductivity at the interface during the charge transfer process. The second process in the medium frequency region is mainly attributed to a faradaic process limited by the adsorption of Li^+ ions on the surface of V_2O_5 electrodes. In the circuit diagram, it is presented by a parallel combination of a resistor, R_3, which is associated with the resistance of the electro-adsorption process and a constant phase element, Q_2, related to the redox active surface phenomenon. W corresponds to the solid-state diffusion of Li^+ ions through the pores of V_2O_5 nanoplates. The final circuit element Q_3 is linked to the charging of a crystalline structure by Li^+ ion intercalation at very low frequencies.[56,57] Additionally, from EIS data analysis, it can also be realized that the overall electrochemical reaction of V_2O_5 electrodes is governed by both diffusion and adsorption processes. Different resistive elements introduced to explain different physical processes are compared in Table S1† for the electrodes. Analyzing the impedance data and previous results it can be concluded that the overall reaction kinetics and electrochromic performances of the V_2O_5-1 material are superior to that of V_2O_5-2 due to its higher surface area. Hence, V_2O_5-1 electrodes were deployed for further measurements related to energy storage.

3.1.4. Scan rate dependent CV and ECSC measurements on V_2O_5 electrodes. Scan rate dependent CV data were collected for both V_2O_5 electrodes, to separate the current contributions that originated from surface- and diffusion-controlled processes. CV measurements at varying scan rates from 2 to 100 mV s^{-1} were performed for the V_2O_5-1 electrode as shown in Fig. 3a. With an increase in the scan rate, the anodic and cathodic peaks shift towards more positive and negative potentials, respectively, which indicates that there is concentration polarization of Li^+ ions at the electrode–electrolyte interface at a higher scan rate.[58] The peak current densities of CV and the scan rates are connected by a relation, $i = a\upsilon^b$, where υ is the sweep rate and a and b are adjustable parameters. When b is close to 1, it suggests that the reaction is governed by a surface-controlled process and for the reactions purely influenced by the diffusion process, b value is nearly 0.5. The inset of Fig. 3a presents $\log(i)$ *vs.* $\log(\upsilon)$ plot and the extracted b value is ~0.74 for the V_2O_5-1 electrode, which implies that the reaction is controlled by both surface and diffusion-controlled

Table 1 Comparison of optical modulation values, switching times and coloration efficiency values of V_2O_5-2 and V_2O_5-1 electrodes

	ΔT (%)		Coloring time (s)		Bleaching time (s)		Coloration eff. ($cm^2\ C^{-1}$)	
Sample	485 nm	1000 nm	485 nm	1000 nm	485 nm	1000 nm	485 nm	1000 nm
V_2O_5-2	28.5	20.4	3	2.4	5.3	3.2	42.96	13.1
V_2O_5-1	35	26.5	2.9	2.1	3.4	2.6	56.51	24.5

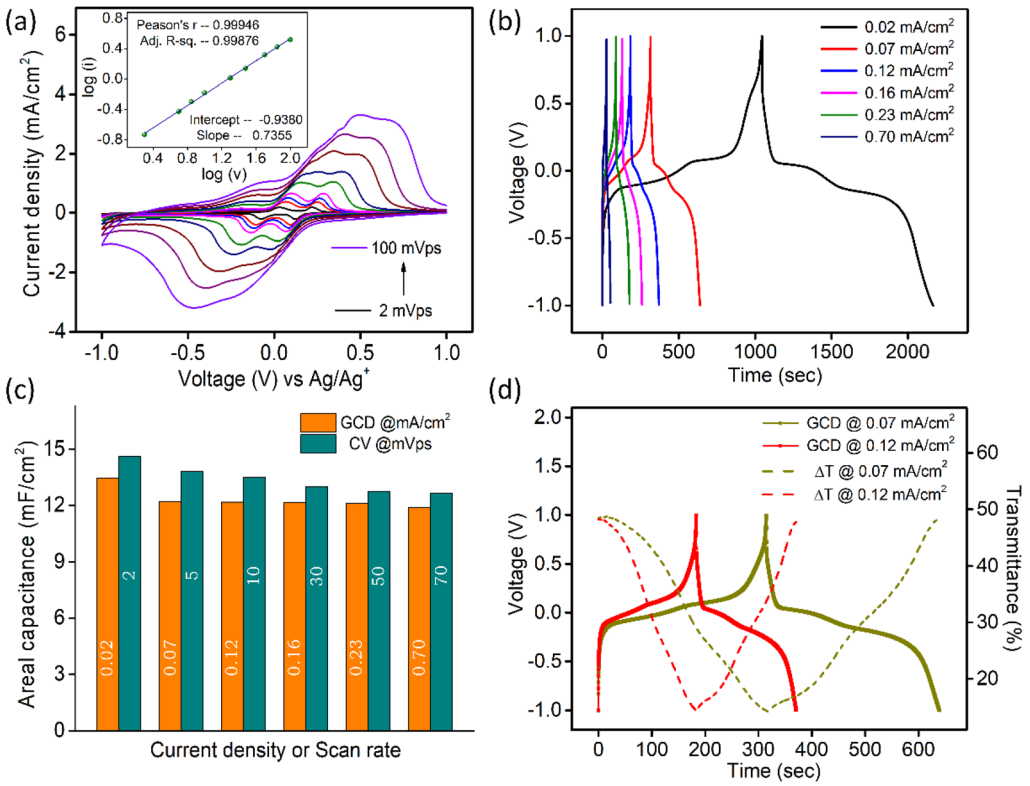

Fig. 3 (a) Scan rate dependent CV data and in the inset log(*i*) *vs.* log(*υ*) plot, (b) GCD plots at different current densities, and (c) comparison of areal capacitances calculated from CV and GCD measurements, (d) *in situ* transmission data at 485 nm synchronized with the GCD data at different current densities.

processes. As presented in Fig. S9a and S9b,† similar measurements were done for the other sample also and the *b* value was found to be ~0.72 suggesting the involvement of similar reaction mechanisms. The current response (i) depends on surface-controlled ($a_1\upsilon$, includes electrical double layer capacitance and surface controlled redox pseudo-capacitance) and diffusion-controlled processes ($a_2\upsilon^{1/2}$), and the total current can be written as a combination of both, as given below:

$$i = a_1\upsilon + a_2\upsilon^{1/2} \quad (3)$$

From the slope and intercept of the graph, $i/\upsilon^{1/2}$ *vs.* $\upsilon^{1/2}$ (Fig. S10a†), a_1 and a_2 coefficients are determined and in the histogram plot of Fig. S10b,† deconvoluted current contributions are presented at different scan rates.[33] With an increase in the scan rate, the contribution of diffusion towards the total current gradually decreases as Li^+ ions do not get sufficient time to intercalate into the material.

Galvanostatic charge–discharge (GCD) data (Fig. 3b) for V_2O_5-1 electrodes were recorded over a potential window of +1 V to −1 V (*vs.* Ag/Ag^+) at varying current densities from 0.02 mA cm^{-2} to 0.7 mA cm^{-2}. The non-linear discharge curves consist of different segments – (a) an IR drop at the start of discharge can be seen due to the internal resistance of the system, (b) a steep linear section is due to the electrical double layer formation and (c) the plateau regions in each segment of the GCD profiles, which arise due to the faradaic reactions, confirming the pseudocapacitive nature of V_2O_5.[59,60] The areal capacitances were calculated from the charge–discharge data according to the standard formula presented as follows:[61]

$$C_a = (I \times \Delta t)/(A \times \Delta V) \quad (4)$$

where I is the discharge current density, Δt is the discharge time, A is the geometric area of working electrodes and ΔV is the IR drop corrected potential window. The highest areal capacitance value, obtained from charge–discharge graphs was 13.44 mF cm^{-2} at a discharge current density of 0.02 mA cm^{-2}. As the discharge current density increases to 0.7 mA cm^{-2} the areal capacitance value decreases to 11.89 mF cm^{-2}, sustaining 88.5% of its capacitance value at 0.02 mA cm^{-2}. Capacitance values for V_2O_5-1 electrodes were also extracted from the CV data based on eqn (5):[62]

$$C_a = \int i dV/(2 \times \upsilon \times A \times \Delta\upsilon) \quad (5)$$

where $\int idV$ is the area under the curve of a CV at a specific scan rate, υ is the scan rate of CV, A is the geometrical area of the electrode and $\Delta\upsilon$ is the potential window in which CV is recorded. The areal capacitance values obtained from CV curves vary from 14.6 to 12.64 mF cm^{-2} with scan rates ranging from 2 to 70 mV s^{-1} and these values are presented in Fig. 3c to confirm the agreement of results derived from both

CV and GCD techniques. *In situ* optical response at 485 nm synchronized with the GCD curves at two different current densities are presented in Fig. 3d. During charging the color of the electrode turns yellow and the corresponding transmittance goes down, while the color gradually changes to bluish gray during discharging and the transmittance goes up. Overall, an optical contrast value of ~34% at 485 nm is exhibited by the V_2O_5-1 electrode upon charging–discharging.

3.2. Positive electrode material (PANI)

PANI consists of two main repeating units, namely reduced benzenoid and oxidized quinoid rings, the relative abundance of which decides the oxidation states and the electrical and optical properties of PANI.[63] PANI exists in three discernible oxidation states. During electrochemical reactions it switches between these states and gives rise to different colors and properties. The three prominent states are as follows: (i) completely reduced leucoemeraldine base (LB) state containing only benzenoid units, which is nearly transparent or light yellow in color, (ii) fully oxidized pernigraniline base (PEB) state (blue in color) consisting of repeated units of benzenoid and quinoid rings and (iii) partially oxidized emeraldine base (EB) state (green in color) which is the most stable form of PANI in ambient atmosphere.[63,64]

3.2.1. Morphology and material characterization. The images of the electrodeposited PANI film at different magnifications, presented in Fig. S11a–c,† show that the film consists of an array of nanofibers of PANI. This porous nature of the film is conducive to the passage of ions and increases the effective contact area of the electrode material with the electrolyte. The chemical thumbprints were manifested by the ATR-FTIR spectrum as shown in Fig. S11d.† The peak at 790 cm^{-1} is due to the out of plane bending vibration of C–H on the benzenoid rings.[18,42] The absorption peak at 1128 cm^{-1} corresponds to the in plane vibration of C–H present in the aromatic rings.[18,41,42] The peaks at 1244 cm^{-1} and 1295 cm^{-1} are attributed to the stretching of the C–N bond of aromatic amine.[18,41,42] The presence of the benzenoid and quinoid ring vibrations of the PANI chains is confirmed by the absorption peaks at 1483 cm^{-1} and 1558 cm^{-1}, respectively.[18,41,42]

3.2.2. Electrochemical measurements on PANI electrodes. Spectroelectrochemical studies of PANI electrodes were performed in a 1 M $LiClO_4$/PC electrolyte in a similar three-electrode setup like V_2O_5 electrodes. The electrochemical reaction that drives the interchange of PANI within its different forms can be given as:[65,66]

$$\text{PANI (LB)} + n\text{ClO}_4^- \leftrightarrow (\text{PANI}^{n+})(\text{ClO}_4^-)_n \text{ (EB)} + ne^-$$

$$(\text{PANI}^{n+})(\text{ClO}_4^-)_n(\text{EB}) + n\text{ClO}_4^- \leftrightarrow (\text{PANI}^{2n+})(\text{ClO}_4^-)_{2n}(\text{PEB}) + ne^- \quad (6)$$

Two pairs of redox peaks arise in the CV profile of PANI due to the doping/dedoping of anions, as presented in Fig. S12.† The first redox couple at lower potentials is attributed to the transition between the LB and EB states and the second pair of peaks is due to the switch between the EB and PEB states as described in the above reactions.

The transmission spectra of PANI electrodes at different potentials (during anodic scan from −1 V to +1 V *vs.* Ag/Ag^+ electrode) are shown in Fig. S13a.† The corresponding film photographs are displayed in Fig. S13b.† The transmission data at two terminal potentials (+1 V and −1 V *vs.* Ag/Ag^+) and the corresponding optical modulation spectra are plotted in Fig. S13c.† The highest change in transmittance in PANI films was found to be nearly 75% at 650 nm. Supporting this, *in situ* optical modulation of the film at 650 nm was measured by CV at a scan rate of 30 mV s^{-1}, as shown in Fig. S13d.†

Scan rate dependent CV data for the PANI electrode are shown in Fig. S14a.† Fig. S14b† presents the $\log(i)$ *vs.* $\log(\upsilon)$ plot and b value comes out to be nearly 0.9. Furthermore, it can be concluded from the plots shown in Fig. S14d† that although the current density of PANI films mostly emerges due to the capacitive process, the contribution also comes from the intercalation of ions into the material. Fig. S15a† presents the GCD data of the PANI film at varying current densities. The areal capacitance value ranges from 13.69 mF cm^{-2} to 11.1 mF cm^{-2} as the current density switches from 0.02 mA cm^{-2} to 0.7 mA cm^{-2}. Similar to the V_2O_5 electrodes, the charge–discharge profiles in this case are also non-linear, which points towards the presence of surface-controlled faradaic processes. The areal capacitance values for PANI films were also extracted from CV curves according to eqn (5). The highest value obtained was 12.3 mF cm^{-2} at a scan rate of 10 mV s^{-1}. The obtained values are compared in Fig. S15b.† With the increase in the scan rate of CV or the current density in charge–discharge, the areal capacitance value decreases due to the inaccessibility of reaction sites of the active material.[67] The *in situ* change in transmittance at 650 nm during charging–discharging of PANI electrodes at different current densities is presented in Fig. S15c.† During charging, the structural units of PANI get oxidized, which demands doping of ClO_4^- ions into the film to maintain the charge balance and this process is accompanied by a transmission drop in PANI films. Removal of electrons along with the movement of charge balancing counter anions causes structural changes in the polymeric chains, leading to the evolution of positively charged polaronic and bipolaronic states. Oxidation of conducting polymers leads to the generation of mid bandgap states and successively creates new lower energy electronic transitions lying in the near-infrared wavelength range.[68,69] During discharging, the reduction of PANI takes place with the simultaneous return of ClO_4^- ions to the solution and the film gains its transparency again.

3.3. Multi-colored electrochromic asymmetric supercapacitor (MECASC)

CV curves collected for both V_2O_5 and PANI electrodes in a 1 M $LiClO_4$/PC electrolyte in a three-electrode setup are presented in Fig. 4a, which sustains our choice of using V_2O_5 as a negative electrode and PANI as a positive electrode in assembling a MECASC for a voltage window up to 2 V. To obtain

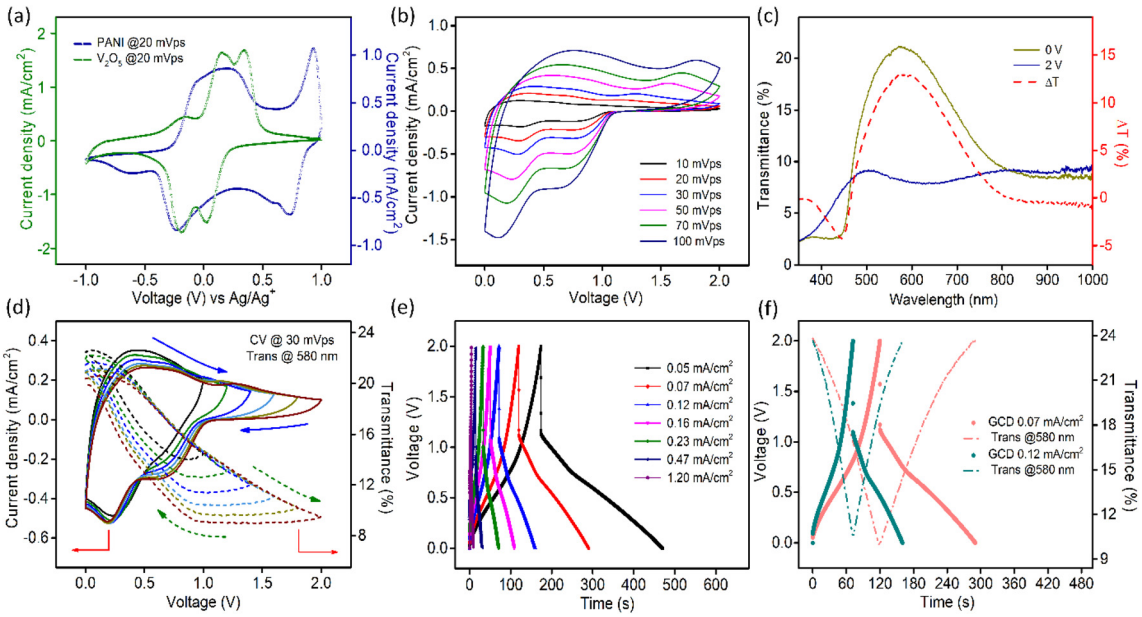

Fig. 4 (a) CV of PANI and V_2O_5 electrodes separately measured in a three-electrode setup in the identical voltage window (±1 V *vs.* Ag/Ag^+) with a 1 M $LiClO_4$/PC electrolyte at a scan rate of 20 mV s^{-1}; (b) CV of the MECASC measured in a two-electrode setup at varying scan rates; (c) transmission spectra of the device at two terminal voltages and the optical modulation spectra (dotted line); and (d) CV at varying potential windows with simultaneous *in situ* transmission changes at 580 nm; (e) GCD profiles at different current densities, and (f) *in situ* transmission changes at 580 nm in harmony with GCD profiles at two different current densities.

better performance from an ASC, the charge balance between its two electrodes should be maintained; *i.e.*, $q^+ = q^-$, where q^+ and q^- correspond to the charges of positive and negative electrodes, respectively, and $q = I \times \Delta t$, where I and Δt are as defined earlier. To do that, the first step was to take the charge–discharge profile of the V_2O_5 electrode at a fixed current density, and then accordingly the electrodeposition time (150 s) of the PANI film was adjusted such that the capacity of the PANI film matches the capacity of V_2O_5.

3.3.1. Spectro-electrochemistry measurements in a two-electrode configuration. Two-electrode CVs of the MECASC were performed in a potential window of 0–2 V at varying scan rates from 10 to 100 mV s^{-1} (Fig. 4b). Semi-rectangular shape of CV along with the presence of redox peaks affirms the synergistic effect of both double layer capacitance and pseudocapacitance.[70] During anodic scan, Li^+ ion intercalates in the V_2O_5 electrode and simultaneously ClO_4^- ions get doped into the PANI film. During discharging, both cations and anions leave the materials and get to the electrolyte besides producing electricity. The half-cell reactions and the overall cell reaction for the whole process can be depicted as:

$$\text{Positive electrode} - (\text{PANI}^{2nx+})(\text{ClO}_4^-)_{2nx} + 2ne^- \leftrightarrow \text{PANI} + 2n\text{ClO}_4^- \quad (7)$$

$$\text{Negative electrode} - \text{Li}_x\text{V}_2\text{O}_5 \leftrightarrow \text{V}_2\text{O}_5 + x\text{Li}^+ + nxe^- \quad (8)$$

$$\text{Overall} - 2n\text{Li}_x\text{V}_2\text{O}_5 + (\text{PANI}^{2nx+})(\text{ClO}_4^-)_{2nx} \leftrightarrow 2n\text{V}_2\text{O}_5 + x\text{PANI} + 2nx\text{LiClO}_4 \quad (9)$$

The contribution of faradaic and surface controlled processes of current was investigated, as shown in Fig. S16a–c.† The plots of $\log(i)$ *vs.* $\log(\upsilon)$ at different voltages are given in Fig. S16a† and the extracted b values signify that the overall reaction is dominated by a surface-controlled capacitive process. The separation of capacitive and diffusive contributions of current at different scan rates is presented in Fig. S16c.†

The transmission spectra of the MECASC were recorded at different voltages during anodic and cathodic scans within the voltage window of 0–2 V, Fig. S17a and b.† Transmission spectra at the end voltages and the optical modulation spectra of the system are shown in Fig. 4c. Transmission modulation reaches a highest value of ~13.5% at 580 nm. At 0 V, the whole system looks yellowish green in color (individually, V_2O_5 and PANI film colors are yellow and yellowish green, respectively) and with the increase in applied bias, PANI and V_2O_5 gradually become oxidized and reduced, respectively. As a consequence, the color of the device changes to dark blue (where V_2O_5 and PANI films change to bluish gray and dark blue color, respectively).

CV profiles (at 30 mV s^{-1} sweep rate) at different working voltage windows are presented in Fig. 4d along with the dynamic changes in transmissions at 580 nm, which are well consistent with the change in current density. As the voltage window increases beyond 1 V, surface-redox reactions start to appear prominently, accompanied by an increase in optical modulation value up to 40% of its initial value as depicted in Fig. 4d. When operational voltage gradually increases from 1 to 2 V, the energy density calculated according to the equation, $E = 1/2 \times CV^2$, elevates from 1.17×10^{-3} to 2.93×10^{-3} mW h cm^{-2}.

GCD measurements (Fig. 4e) of the MECASC module were performed at different current densities ranging from 0.05 to 1.2 mA cm^{-2} within the operational voltage window of 2 V. The presence of nonlinearity in GCD profiles indicates the existence of faradaic reactions in PANI and V_2O_5. The areal capacitance touches a maximum value of 12.27 mF cm^{-2} at a current density of 0.05 mA cm^{-2} with an energy density of 2.21×10^{-3} mW h cm^{-2}. At a 24 times higher current density of 1.2 mA cm^{-2}, 58.2% areal capacitance value *i.e.*, 7.14 mF cm^{-2} can be retained compared to that at 0.05 mA cm^{-2} and the energy density decreases to 5.7×10^{-4} mW h cm^{-2}. Fig. 4f presents the optical modulation synced with GCD profiles at two different current densities. Optical modulation at 580 nm reduces from 13.7% to 12.9% with an increase in the current density from 0.07 to 0.12 mA cm^{-2} with a simultaneous decrement in areal capacitance from 10.63 to 9.52 mF cm^{-2}. The probable reason behind this is the inaccessibility of active electrode materials for charge storage as there is a limitation in the migration of ionic species with the increase in the current density.[71]

Fig. 5a shows the GCD profile of the MECASC at a current density of 0.12 mA cm^{-2}. The photographs of the module are presented in Fig. 5b at different instants of charging and discharging as shown by the red circles in the GCD curve in Fig. 5a. This well coordinated behavior of color changes (yellowish green, dark green, greenish blue, blue and dark blue) during charging–discharging of the electrode helps to uniquely identify the state of charge of the system. To further understand the performance of the MECASC system, the switching times and the coloration efficiency were calculated. Switching times were determined according to the description previously given in section 3.1.2, by applying potentials alternating

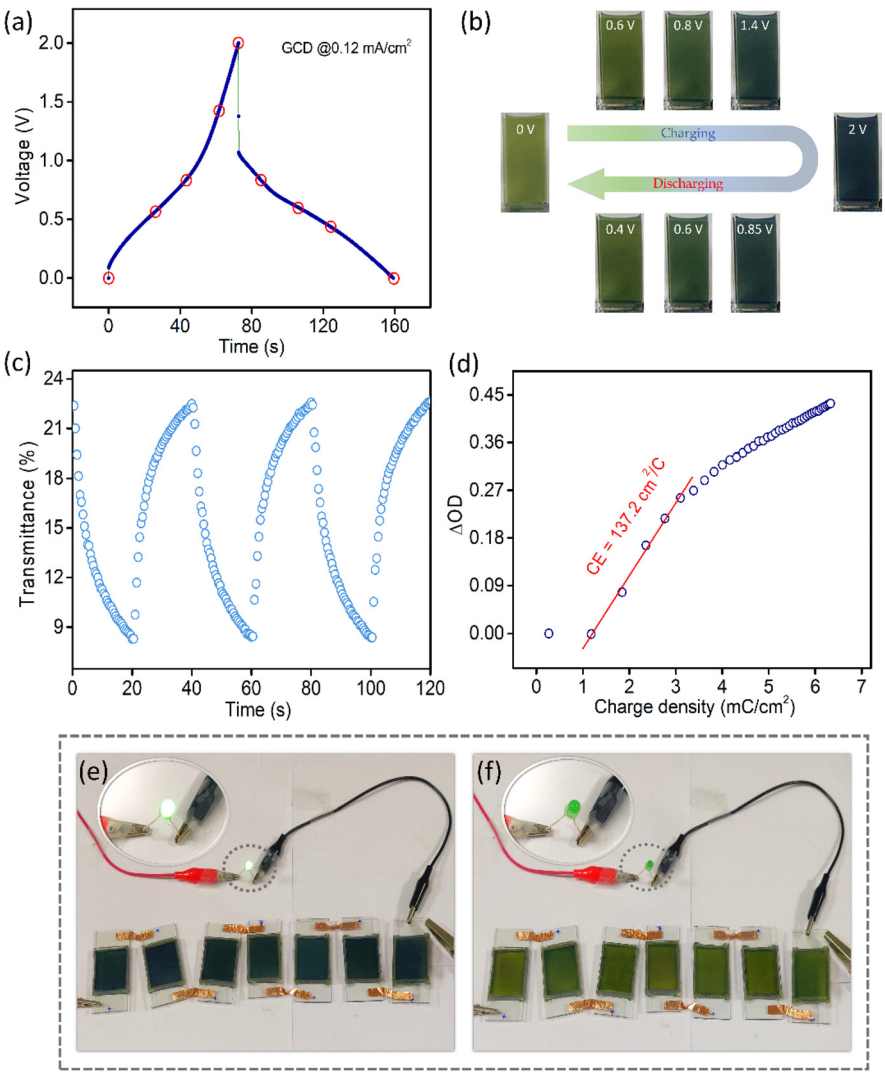

Fig. 5 (a) GCD profile of the MECASC at a current density of 0.12 mA cm^{-2}, (b) photographs of the system at different voltages during charging and discharging as assigned by the red circles in (a); (c) switching times of the module at 580 nm by applying 0 V and 2 V potential alternatively with 20 s interval; (d) coloration efficiency of the system at 580 nm; and photographs demonstrate (e) charged and (f) discharged states of the devices, connected in series; insets show the state of the LED in both cases.

between 0 V and 2 V. Calculated coloration and bleaching times of the system were 16.4 s and 12.9 s, respectively. Furthermore, the coloration efficiency (CE) was calculated at 580 nm wavelength according to eqn (2) and a high CE value of 137.2 cm^2 C^{-1} was obtained for the module.

Cycling performance is a measure of the life span of a device for practical applications. By conducting the cycling stability measurement at a high current density of 1 mA cm^{-2}, it is observed that the supercapacitor can sustain nearly 50% of its initial capacitance value after 7000 cycles (Fig. S18a†). This kind of capacity decay is quite common among V_2O_5 electrodes.[50,53,72,73] The galvanostatic charge–discharge (GCD) curves of the module at a current density of 0.12 mA cm^{-2} along with the dynamic change of its transmission at 580 nm wavelength before and after cycling are presented in Fig. S18b.† After cycling, the transmission modulation value at 580 nm reduces by ~18.47% of its initial value. There is a lowering in transmittance of the bleached state, which may be caused due to the trapped charge inside the electrodes because of repeated cycling.[74,75] The morphologies of both V_2O_5 and PANI films were examined by the FESEM technique. Fig. S19 and S20† present the FESEM images of V_2O_5 and PANI electrodes, respectively, at different magnifications (10 μm and 1 μm) before and after cycling. For the V_2O_5 electrode, dark patches were noticed on the films after cycling as presented in Fig. S19c and S19d,† which are absent in the image, illustrated in Fig. S19a and S19b† before cycling. The patches could be the portions of the electrode from where chunks of electrode materials were peeled off during cycling. Fig. S19b and S19d† illustrate these aspects with better clarity. This occurs due to the mechanical stress generated during ion intercalation–deintercalation,[76] causing capacity fading for V_2O_5-based materials as mentioned in previous reports.[30,77,78] Additionally, no visible color change of the electrolyte was noted after the cycling test. According to other literature reports, V_2O_5 tends to dissolve in an aqueous electrolyte during cycling;[47,51] in contrast, organic electrolytes effectively decrease the dissolution of V_2O_5 and increase the stability of the electrodes.[51] From Fig. S20a and S20c,† not much change in the PANI electrode is observed before and after cycling. A closer inspection reveals that the diameters of the pores in the PANI film increased after cycling as presented in Fig. S20b and S20d.†

Prototypes of the MECASC (2.5 cm × 4 cm) were assembled to demonstrate the practical applicability. The devices were connected in series, which lit up the green LED for almost 7 min (video provided in the ESI†). The photograph of the devices is presented in Fig. 5e in their charged states with a glowing green LED. Fig. 5f shows the discharged state of the devices with a yellowish green color and an LED in the off state.

4. Conclusion

MOF-derived V_2O_5 has been successfully synthesized and employed as an electrochromic electrode, which shows large optical modulations with very fast switching times and decent coloration efficiencies. Later, the V_2O_5 film was used as the negative electrode for the fabrication of a multicolored electrochromic asymmetric supercapacitor alongside an electrodeposited PANI film, which was deployed as the positive electrode. Owing to its multiple-colored states at different stages of charging and discharging, it enables the direct determination of its energy storage level with the naked eye. As an electrochromic energy storage device, it demonstrates a high coloration efficiency of 137.2 cm^2 C^{-1} and an areal capacitance of 12.27 mF cm^{-2} with an energy density of 2.21 × 10^{-3} mW h cm^{-2} at a current density of 0.05 mA cm^{-2}. Moreover, this operates as an energy-efficient EC device by eliminating the requirement of energy during bleaching as it recycles the energy stored during charging. In a nutshell, this work is a new stride towards the intelligent automation of energy storage devices.

Conflicts of interest

The authors declare no financial interest.

Acknowledgements

We want to thank Mr Shriniwas Deo from the CSIR-National Chemical Laboratory (CSIR-NCL, Pune) for his help with the XPS measurement. We sincerely thank Prof. Sujit K. Ghosh and his student Dr Subhajit Dutta from the Department of Chemistry, IISER Pune, for helping us with the gas adsorption measurements of the samples. A. D. thanks Dr Sattwick Haldar for helping with the fitting of adsorption data. A. D. acknowledges Dr Atikur Rahman and his students Mr Gokul M. A. and Mr Tamaghna Chowdhury from the Department of Physics, IISER Pune, for helping with the tube furnace setup in their lab. A. D. thanks Mr Soumodip Sur for his cooperation during the work. A. D. acknowledges the INSPIRE fellowship from the DST, India. R. N. acknowledges funding from the Department of Science Technology, India, through the INSPIRE faculty scheme (DST/INSPIRE/04/2017/002761). M. O. T. is indebted to the DST-SERB (CRG/2020/002549), the DST-WTI (DST/TMD-EWO/WTI/2K19/EWFH/2019/272) and the DST-HFC (DST/TMD/HFC/2K18/58) for financial support.

References

1 A. Eftekhari, *ACS Sustainable Chem. Eng.*, 2019, **7**, 5602–5613.
2 Q. Zhang, B. He, L. Tang, Z. Zhou, L. Kang, J. Sun, T. Zhang, Q. Li, C. Li, J. Zhao, Z. Zhang, L. Wei and Y. Yao, *Adv. Funct. Mater.*, 2019, **29**, 1808889.
3 A. Fakharuddin, R. Jose, T. M. Brown, F. Fabregat-Santiago and J. Bisquert, *Energy Environ. Sci.*, 2014, **7**, 3952–3981.
4 S. Cavaliere, S. Subianto, I. Savych, D. J. Jones and J. Rozière, *Energy Environ. Sci.*, 2011, **4**, 4761–4785.

5 J. Yuan, M. Qiu, X. Hu, Y. Liu, G. Zhong, H. Zhan and Z. Wen, *ACS Nano*, 2022, **16**, 14807–14818.
6 Y. Liu, X. Hu, J. Li, G. Zhong, J. Yuan, H. Zhan, Y. Tang and Z. Wen, *Nat. Commun.*, 2022, **13**, 663.
7 L. J. Wang, M. F. El-Kady, S. Dubin, J. Y. Hwang, Y. Shao, K. Marsh, B. McVerry, M. D. Kowal, M. F. Mousavi and R. B. Kaner, *Adv. Energy Mater.*, 2015, **5**, 1500786.
8 P. Simon and Y. Gogotsi, *Nat. Mater.*, 2008, **7**, 845–854.
9 T. Zhu, Y. Yang, Y. Liu, R. Lopez-Hallman, Z. Ma, L. Liu and X. Gong, *Nano Energy*, 2020, **78**, 105397.
10 P. Xie, W. Yuan, X. Liu, Y. Peng, Y. Yin, Y. Li and Z. Wu, *Energy Storage Mater.*, 2021, **36**, 56–76.
11 Y. Huang, M. Zhu, Z. Pei, Q. Xue, Y. Huang and C. Zhi, *J. Mater. Chem. A*, 2016, **4**, 1290–1297.
12 Y. Jiang, M. Cheng, R. Shahbazian-Yassar and Y. Pan, *Adv. Mater. Technol.*, 2019, **4**, 1900691.
13 X. Liang, L. Zhao, Q. Wang, Y. Ma and D. Zhang, *Nanoscale*, 2018, **10**, 22329–22334.
14 Q. Guo, X. Zhao, Z. Li, D. Wang and G. Nie, *Chem. Eng. J.*, 2020, **384**, 123370.
15 J. Chen, Z. Wang, Z. Chen, S. Cong and Z. Zhao, *Nano Lett.*, 2020, **20**, 1915–1922.
16 Z. Lu, X. Zhong, X. Liu, J. Wang and X. Diao, *Phys. Chem. Chem. Phys.*, 2021, **23**, 14126–14145.
17 H. Wang, C.-J. Yao, H.-J. Nie, L. Yang, S. Mei and Q. Zhang, *J. Mater. Chem. C*, 2020, **8**, 15507–15525.
18 Y. Zhong, Z. Chai, Z. Liang, P. Sun, W. Xie, C. Zhao and W. Mai, *ACS Appl. Mater. Interfaces*, 2017, **9**, 34085–34092.
19 Q. Guo, J. Li, B. Zhang, G. Nie and D. Wang, *ACS Appl. Mater. Interfaces*, 2019, **11**, 6491–6501.
20 Q. Guo, X. Zhao, Z. Li, B. Wang, D. Wang and G. Nie, *ACS Appl. Energy Mater.*, 2020, **3**, 2727–2736.
21 N. Kobayashi, S. Miura, M. Nishimura and H. Urano, *Sol. Energy Mater. Sol. Cells*, 2008, **92**, 136–139.
22 J. Padilla, V. Seshadri, T. F. Otero and G. A. Sotzing, *J. Electroanal. Chem.*, 2007, **609**, 75–84.
23 J. Wang, L. Zhang, L. Yu, Z. Jiao, H. Xie, X. W. Lou and X. W. Sun, *Nat. Commun.*, 2014, **5**, 4921.
24 S. Mishra, P. Yogi, P. R. Sagdeo and R. Kumar, *ACS Appl. Energy Mater.*, 2018, **1**, 790–798.
25 G. Cai, P. Darmawan, X. Cheng and P. S. Lee, *Adv. Energy Mater.*, 2017, **7**, 1602598.
26 W. Zhang, H. Li, W. W. Yu and A. Y. Elezzabi, *Small Sci.*, 2021, **1**, 2100040.
27 S. B. Singh, D. T. Tran, K.-U. Jeong, N. H. Kim and J. H. Lee, *Small*, 2022, **18**, 2104462.
28 H. Liang, R. Li, C. Li, C. Hou, Y. Li, Q. Zhang and H. Wang, *Mater. Horiz.*, 2019, **6**, 571–579.
29 L. Zhao, J. Kuang, W. Zhuang, J. Chao, W. Liao, X. Fu, C. Li, L. Ye and H. Liu, *Nanotechnology*, 2021, **33**, 054001.
30 S. Zhang, S. Chen, Y. Luo, B. Yan, Y. Gu, F. Yang and Y. Cao, *J. Alloys Compd.*, 2020, **842**, 155882.
31 D. Majumdar, M. Mandal and S. K. Bhattacharya, *ChemElectroChem*, 2019, **6**, 1623–1648.
32 M. M. Margoni, S. Mathuri, K. Ramamurthi, R. R. Babu, V. Ganesh and K. Sethuraman, *Appl. Surf. Sci.*, 2018, **449**, 193–202.
33 A. Dewan, S. Sur, R. Narayanan and M. O. Thotiyl, *ChemElectroChem*, 2022, **9**, e202200001.
34 R. R. Salunkhe, Y. V. Kaneti and Y. Yamauchi, *ACS Nano*, 2017, **11**, 5293–5308.
35 Y.-S. Hsiao, C.-W. Chang-Jian, W.-L. Syu, S.-C. Yen, J.-H. Huang, H.-C. Weng, C.-Z. Lu and S.-C. Hsu, *Appl. Surf. Sci.*, 2021, **542**, 148498.
36 T. Q. He, J. H. Li, Z. Z. Luo, Y. Q. Zhang, Y. Y. Zhao, X. T. Zhang and Y. J. Chen, *ChemElectroChem*, 2022, **9**, e202200178.
37 Y. Ding, Y. Peng, W. Chen, Y. Niu, S. Wu, X. Zhang and L. Hu, *Appl. Surf. Sci.*, 2019, **493**, 368–374.
38 T. Kim, H. Kim, T.-S. You and J. Kim, *J. Alloys Compd.*, 2017, **727**, 522–530.
39 W. Li, J. Wang, J. Chen, K. Chen, Z. Wen and A. Huang, *Small*, 2022, **18**, 2202018.
40 F. Carson, J. Su, A. E. Platero-Prats, W. Wan, Y. Yun, L. Samain and X. Zou, *Cryst. Growth Des.*, 2013, **13**, 5036–5044.
41 Y. Mohd, R. Ibrahim and M. F. Zainal, Presented in part at the 2012 IEEE Symposium on Humanities, Science and Engineering Research, Kuala Lumpur, 24–27 June 2012, 2012.
42 P. Yilmaz, M. Magni, S. Martinez, R. M. Gonzalez Gil, M. Della Pirriera and M. Manca, *ACS Appl. Energy Mater.*, 2020, **3**, 3779–3788.
43 G. Férey, C. Mellot-Draznieks, C. Serre, F. Millange, J. Dutour, S. Surblé and I. Margiolaki, *Science*, 2005, **309**, 2040–2042.
44 S. Biswas, S. Couck, M. Grzywa, J. F. M. Denayer, D. Volkmer and P. Van Der Voort, *Eur. J. Inorg. Chem.*, 2012, **2012**, 2481–2486.
45 W.-C. Fang, *J. Phys. Chem. C*, 2008, **112**, 11552–11555.
46 Y. Chen, K. Muthukumar, L. Leban and J. Li, *Electrochim. Acta*, 2020, **330**, 135200.
47 H. Liu, W. Zhu, D. Long, J. Zhu and G. Pezzotti, *Appl. Surf. Sci.*, 2019, **478**, 383–392.
48 M. Sathiya, A. S. Prakash, K. Ramesha, J. M. Tarascon and A. K. Shukla, *J. Am. Chem. Soc.*, 2011, **133**, 16291–16299.
49 C. Y. Foo, A. Sumboja, D. J. H. Tan, J. Wang and P. S. Lee, *Adv. Energy Mater.*, 2014, **4**, 1400236.
50 M. Li, G. Sun, P. Yin, C. Ruan and K. Ai, *ACS Appl. Mater. Interfaces*, 2013, **5**, 11462–11470.
51 H. Zhang, X. Han, R. Gan, Z. Guo, Y. Ni and L. Zhang, *Appl. Surf. Sci.*, 2020, **511**, 145527.
52 B. D. Boruah, B. Wen and M. De Volder, *Nano Lett.*, 2021, **21**, 3527–3532.
53 J. Yang, T. Lan, J. Liu, Y. Song and M. Wei, *Electrochim. Acta*, 2013, **105**, 489–495.
54 A. Dewan, S. Haldar and R. Narayanan, *J. Solid State Electrochem.*, 2021, **25**, 821–830.
55 M. Holzapfel, A. Martinent, F. Alloin, B. Le Gorrec, R. Yazami and C. Montella, *J. Electroanal. Chem.*, 2003, **546**, 41–50.

56 S. K. Meher, P. Justin and G. Ranga Rao, *Nanoscale*, 2011, **3**, 683–692.
57 V. Lvovich, in *Impedance Spectroscopy: Applications to Electrochemical and Dielectric Phenomena*, John Wiley & Sons, 2012, pp. 281–318, DOI: **10.1002/9781118164075.ch12**.
58 H. Lee, V. S. Kumbhar, J. Lee, Y. Choi and K. Lee, *Electrochim. Acta*, 2020, **334**, 135618.
59 Y. Zhang, J. Zheng, Y. Zhao, T. Hu, Z. Gao and C. Meng, *Appl. Surf. Sci.*, 2016, **377**, 385–393.
60 B. Pandit, D. P. Dubal, P. Gómez-Romero, B. B. Kale and B. R. Sankapal, *Sci. Rep.*, 2017, **7**, 43430.
61 J. Pan, R. Zheng, Y. Wang, X. Ye, Z. Wan, C. Jia, X. Weng, J. Xie and L. Deng, *Sol. Energy Mater. Sol. Cells*, 2020, **207**, 110337.
62 M. Qiu, P. Sun, L. Shen, K. Wang, S. Song, X. Yu, S. Tan, C. Zhao and W. Mai, *J. Mater. Chem. A*, 2016, **4**, 7266–7273.
63 M. Beygisangchin, S. Abdul Rashid, S. Shafie, A. R. Sadrolhosseini and H. N. Lim, *Polymers*, 2021, **13**, 2003.
64 S. F. Kuchena and Y. Wang, *ACS Appl. Energy Mater.*, 2020, **3**, 11690–11698.
65 X. Wu, Q. Wang, W. Zhang, Y. Wang and W. Chen, *Synth. Met.*, 2016, **220**, 494–501.
66 K. Xu, Q. Zhang, Z. Hao, Y. Tang, H. Wang, J. Liu and H. Yan, *Sol. Energy Mater. Sol. Cells*, 2020, **206**, 110330.
67 K. Zhou, H. Wang, J. Jiu, J. Liu, H. Yan and K. Suganuma, *Chem. Eng. J.*, 2018, **345**, 290–299.
68 A. L. Dyer, A. M. Österholm, D. E. Shen, K. E. Johnson and J. R. Reynolds, in *Electrochromic Materials and Devices*, ed. R. J. Mortimer, D. R. Rosseinsky and P. M. S. Monk, Wiley-VCH Verlag GmbH & Co. KGaA, 2015, pp. 113–184.
69 W. T. Neo, M. H. Chua and J. W. Xu, in *Electrochromic Smart Materials: Fabrication and Applications; Smart Materials Series*, ed. J. W. Xu, M. H. Chua and K. W. Shah, The Royal Society of Chemistry, 2019, pp. 22–50.
70 K. Subramani, N. Sudhan, R. Divya and M. Sathish, *RSC Adv.*, 2017, **7**, 6648–6659.
71 G. Cai, P. Darmawan, M. Cui, J. Wang, J. Chen, S. Magdassi and P. S. Lee, *Adv. Energy Mater.*, 2016, **6**, 1501882.
72 F. Azadian and A. C. Rastogi, *Electrochim. Acta*, 2020, **330**, 135339.
73 B. Saravanakumar, K. K. Purushothaman and G. Muralidharan, *ACS Appl. Mater. Interfaces*, 2012, **4**, 4484–4490.
74 J. Guo, M. Wang, X. Diao, Z. Zhang, G. Dong, H. Yu, F. Liu, H. Wang and J. Liu, *J. Phys. Chem. C*, 2018, **122**, 19037–19043.
75 E. Hopmann, H. Li and A. Y. Elezzabi, *RSC Adv.*, 2019, **9**, 32047–32057.
76 B. Saravanakumar, K. K. Purushothaman and G. Muralidharan, *J. Electroanal. Chem.*, 2015, **758**, 111–116.
77 W. Zhang, H. Li, M. Al-Hussein and A. Y. Elezzabi, *Adv. Opt. Mater.*, 2020, **8**, 1901224.
78 E. Umeshbabu and G. Ranga Rao, *J. Colloid Interface Sci.*, 2016, **472**, 210–219.